

## A promising hydroxyapatite/graphene hybrid nanocomposite for methylene blue dye's removal in wastewater treatment

Mohamed A. Hassan<sup>1</sup>, Ahmad M. Mohammad<sup>2,\*</sup>, Taher A. Salaheldin<sup>1,3</sup>, Bahgat E. El-Anadouli<sup>2,\*</sup>

<sup>1</sup> Nanotechnology and Advanced Materials Central Laboratory, Agriculture Research Center, Giza, Egypt

<sup>2</sup> Chemistry Department, Faculty of Science, Cairo University, PO 12613 Giza, Egypt

<sup>3</sup> Nanotechnology Research Centre, British University in Egypt, Egypt

\*E-mail: ammohammad@cu.edu.eg, bahgat@sci.cu.edu.eg

Received: 17 February 2018 / Accepted: 12 April 2018 / Published: 5 July 2018

A novel hydroxyapatite/graphene hybrid nanocomposite (HAp/G) was developed as a competent adsorbent for the removal of methylene blue (MB) dye in wastewater treatment. The adsorption was pursued in a batch process that followed pseudo-second-order kinetics. Several techniques including the high resolution transmission electron microscopy (HR-TEM), energy dispersive X-ray analysis (EDX), X-ray diffraction (XRD), Fourier transform infrared spectrophotometry (FTIR) and Zeta potential (Electrokinetic potential) measurements were employed to evaluate the topography, composition, crystal structure, functionality and stability of the developed sorbent. The equilibrium concentration of MB was estimated using UV-Vis spectrophotometry. The impact of MB's initial concentration, HAp/G's dosage and solution pH on the adsorption capacity of HAp/G was investigated. Interestingly, superior removal efficiencies (up to 99.9%) for MB were obtained using HAp/G. Typically, the maximum sorption capacity ( $q_m$ ) of HAp/G to MB was 333.3 mg/g, which excelled several previously-reported achievements at other sorbents. The harmony of data fitting with the Langmuir isotherm was successful.

**Keywords:** Wastewater; Graphene composites; Adsorption; Dyes; Langmuir.

### 1. INTRODUCTION

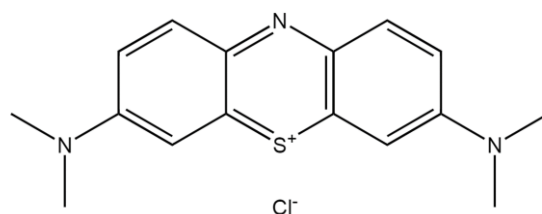
The urgency for sustaining abundant clean water supplies for domestic use, irrigation and industry is growing parallel to the global desire to switch into renewability, particularly with the rapid growth of world population that hampers the sole dependence on natural resources. The international fund for agricultural development (IFAD) projected two-thirds of the world population encountering stresses by water scarcity by 2025 [1]. This stimulated a sincere attention to groundwater which is

often less expensive, more convenient and less susceptible to pollution than surface (river, lake, wetland, or ocean) water. Alternatively, effort is expended intensively to remediate industrial effluents for useful purposes other than drinking. In this context, dyes' manufacturing that constitutes the standard backbone of textile, paper, paint, rubber, plastics, leather, cosmetics, food, and pharmaceutical industries was challenging [2]. Discharging of colored dyes even with minute amounts into water streams without proper treatments may furnish water with an undesirable coloration and a dramatic increase in chemical oxygen demand and toxicity, particularly if these dyes degraded into carcinogenic adducts [3-5]. Roughly estimated, the number of available commercial synthetic dyes and pigments exceeds 10 thousands with a production capacity approaching  $7 \times 10^5$  tonnes/year [6]. The problem of this massive production depicts in the significant (10–15%) loss of these dyes during applications in the effluent of these industries [6, 7]. The aromatic nature of synthetic dyes (highly water soluble), in particular, inspires a harmful impact to aquatic animals and plants; necessitating a proper remediation for these effluents before discharging into water bodies. In this regard, several biological, chemical and physical protocols has been assigned for dyes; removal in wastewater treatment [6]. The biological (aerobic or anaerobic) treatment involved an accumulation and a consequent biodegradation of these dyes on different microorganism as yeasts, fungi, bacteria and algae. However, this treatment was not convenient for large fluxes of industrial treatments as the dyes' removal efficiency was low and depended on climate change and the reactor's size [8]. On the other hand, the chemical treatment targeted a coagulation/flocculation of dyes with chemical agents to end up with a massive chemical sludge requiring a further remediation [9]. Alternatively, the physical treatments included filtration, reverse osmosis and adsorption which exhibited a superior dyes' removal efficiency at cheap costs and a simple processing [10]. The adsorption technique featured, moreover, low sensitivity to toxic pollutants; avoiding the complications associating physical membrane-based technologies [11-13]. For this excellence, research is growing to develop new adsorbents of low cost and high effectiveness for dyes' removal in wastewater treatment. Interesting sorbents included the natural and modified clay, chitosan, zeolites, fly ash, coal, paper mill sludge and agricultural or industrial wastes as replacements for the traditional activated carbon that typically required complications in manufacturing and regeneration [6].

Recently, hydroxyapatite (HAp– $\text{Ca}_{10}(\text{PO}_4)_6(\text{OH})_2$ ), the main inorganic calcium phosphate mineral component of human bones and teeth) has different potential applications in electrochemical deposition for biomedical aspects and in wastewater treatment owing to its greenness and simple low-cost production with good dispersibility, high specific surface area, abundant hydroxyl groups, low water solubility and high stability under reducing and oxidizing conditions [14-18]. We also could successfully synthesize unmodified HAp nanorods and chitosan (Cs)-modified hydroxyapatite (HApCs) nanorods with outstanding removal's efficiencies for heavy metal ions of cadmium and lead from wastewater streams [19, 20].

Alternatively, convoying with the advanced revolution in nanoscience [21-24] and the innovation utilized carbon-based nanomaterials, graphene (the thinnest material in universe and the two-dimensional carbon sheet with one atom thickness) nanocomposites and hybrids have attracted increasing attention for real applications in energy, electrochemical, catalytic and environmental aspects [25, 26]. The diversity in graphene's applications was inspired from the unique properties it

owed as the high theoretical surface area ( $2630 \text{ m}^2/\text{g}$ ), enhanced mobility ( $200,000 \text{ cm}^2 \text{ V}^{-1} \text{ s}^{-1}$  at carrier density of  $\sim 10^{12} \text{ cm}^{-2}$ ), improved electrical conductivity at room temperature ( $10^6 \text{ s cm}^{-1}$ ), high mechanical properties (Young's modulus of  $\sim 1 \text{ TPa}$  and breaking strength of  $42 \text{ N m}^{-1}$ ) and excellent thermal conductivity ( $\sim 5000 \text{ W m}^{-1} \text{ K}^{-1}$ ) [27-31]. Environmentally, graphene composites have shown excellent activity for the adsorption/removal of arsenic and chromium ions from wastewater [32, 33]. Carbon nanotube–graphene hybrid aerogels were also very promising in the removal of organic dyes in water purification [34]. Hence, we were motivated to compile the virtues of HAp and graphene in a single hybrid (abbreviated HAp/G) nanocomposite for the removal of organic dyes in wastewater treatments. The removal of methylene blue (MB – also known as methylthioninium chloride – Scheme 1) dye, which attends intensively in industrial waste streams was employed for marking the sorption efficiency and capacity of the hybrid HAp/G nanocomposite (HAp/G).



**Scheme 1.** Methylene blue (MB). IUPAC name: 3,7-bis(Dimethylamino)-phenothiazin-5-ium chloride.

## 2. MATERIALS AND METHODS

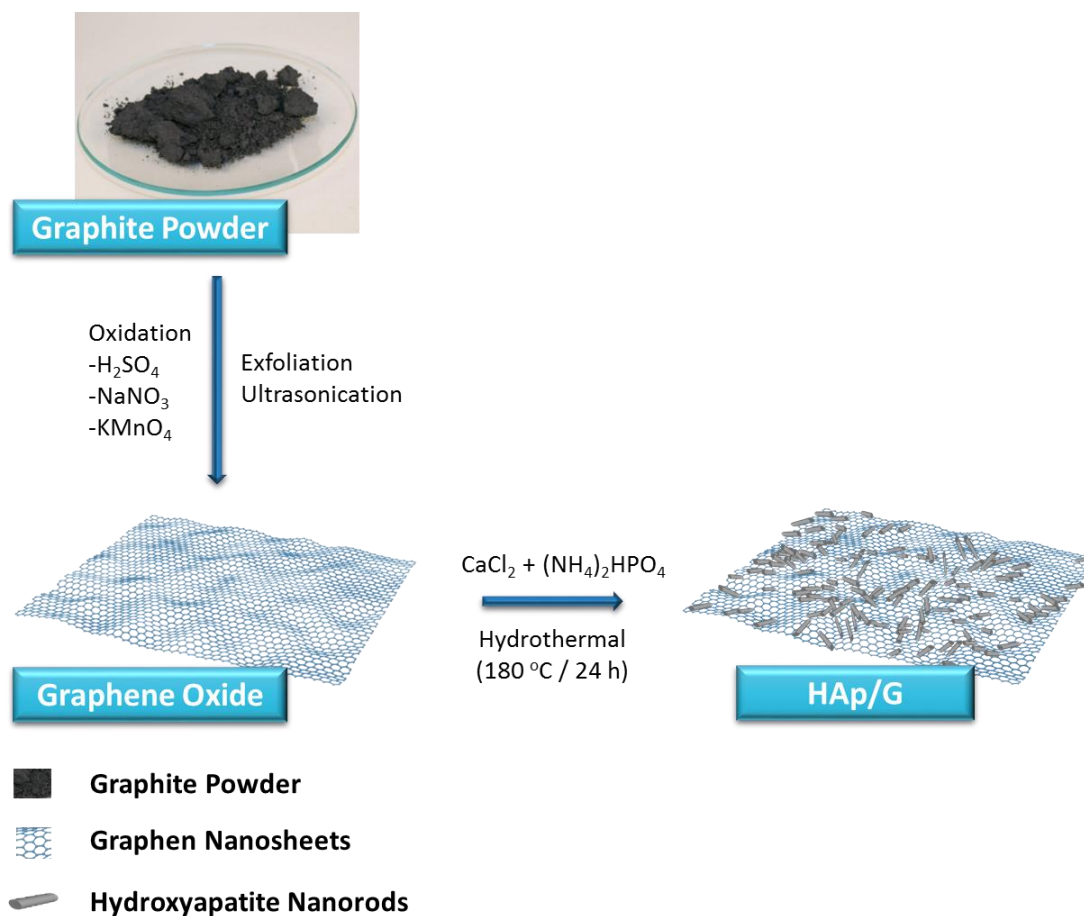
### 2.1 Preparation and materials characterization

All chemicals employed in this investigation including graphite powder (C, -200 mesh, 99.9999% - Alfa Aesar), sulfuric acid ( $\text{H}_2\text{SO}_4$ , 95–97%, Sigma–Aldrich), sodium nitrate ( $\text{NaNO}_3$ , 99.5%, Sigma), potassium permanganate ( $\text{KMnO}_4$ , 99.0%, Sigma–Aldrich), hydrogen peroxide ( $\text{H}_2\text{O}_2$ , 35%, Alfa Aesar), phosphoric acid ( $\text{H}_3\text{PO}_4$ , Sigma–Aldrich), calcium nitrate ( $\text{Ca}(\text{NO}_3)_2 \cdot 4\text{H}_2\text{O}$ , Sigma–Aldrich), hydrochloric acid ( $\text{HCl}$ , 38%, Sigma–Aldrich), sodium hydroxide pellets anhydrous ( $\text{NaOH}$ , 98%, Sigma–Aldrich) and MB ( $\text{C}_{16}\text{H}_{18}\text{ClN}_3\text{S} \cdot 2\text{H}_2\text{O}$ , Rankem) were of analytical grade purity and were, hence, used without prior treatments.

Graphene oxide (GO – formerly called graphitic oxide or graphitic acid) nano-sheets was synthesized as a precursor of graphene (G) using a modified Hummers method [35, 36]. Briefly, 5.0 g graphite powder was dissolved in 175 mL sulfuric acid containing 3.75 g sodium nitrate at  $70^\circ\text{C}$  under continuous stirring for 45 min (or until attaining a complete dissolution). The temperature was lowered below  $5^\circ\text{C}$  while maintaining a vigorous agitation before adding 30 g  $\text{KMnO}_4$  (as an oxidizing agent) slowly into the mixture. The addition of  $\text{KMnO}_4$  was controlled carefully to maintain the temperature below  $20^\circ\text{C}$ . The ice-bath was then removed and the suspension was left at  $35^\circ\text{C}$  for 5 h (sometimes left overnight) under stirring. The reaction progress accompanies a gradual thickening (brownish grey paste formation) of the mixture with a gas evolution. Next, 184 mL of water was slowly dropped into

the paste under stirring, causing violent effervescence and an increase in temperature to 98°C. The diluted suspension (brown in color) was maintained at this temperature for 15 min. A further dilution for the suspension with 560 mL warm water was maintained before adding 10 mL (5% H<sub>2</sub>O<sub>2</sub>) to reduce the residual permanganate and manganese dioxide to colorless soluble manganese sulfate. The treatment with H<sub>2</sub>O<sub>2</sub> turned the suspension's color into bright yellow. The suspension was centrifuged (in a yellowish-brown filter cake) while being warmed to avoid precipitation of the slightly soluble salt of mellitic acid which was formed in a side reaction. After washing the yellowish-brown filter cake three times with warm water and 10% HCl, the paste was dried at 50°C to obtain the dark brown nanosheet of GO.

The HAp/G nanocomposite was synthesized (Scheme 2) by suspending 30 mg of the prepared GO in 30 mL H<sub>2</sub>O in an ultrasonic bath for 30 min before adding 0.074 g CaCl<sub>2</sub>. In a separate flask, 0.040 g of (NH<sub>4</sub>)<sub>2</sub>HPO<sub>4</sub> was dissolved in another 30 mL deionized (DI) water and gradually added to GO-containing solution maintaining the pH adjusted at 10 using 30% ammonium hydroxide. The mixture was then heated in a stainless steel Teflon lined autoclave at 180°C for 24 h. After that, the HAp/G nanocomposite was separated by successive centrifugation and washing in DI water and ethanol and finally by drying at 70°C overnight [37].



**Scheme 2.** A schematic for the preparation of HAp/G nanocomposite.

The diversity of tools employed in this study to characterize the developed HAp/G hybrid nanocomposite could successfully provide a detailed overview mapping its morphology, composition, crystal structure, functionality and expected adsorption capacity. Morphologically, compositionally, and structurally, the high resolution transmission electron microscopy (HR-TEM, Tecnai G20, FEI, Netherland) with the attached energy dispersive X-ray spectroscope (EDX) could inspect the surface topography and bulk composition of the HAp/G nanocomposite revealing interesting information about the material's crystallinity. In this investigation, particles were suspended onto 200 mesh Cu grids coated with a carbon film. The bright field and diffraction pattern imaging techniques were employed at 200 kV using LaB<sub>6</sub> electron source gun. The crystal phase was identified using X-ray diffractometer (XRD – X'Pert PRO PANalytical, Netherland) operated at 45 kV and 30 mA using filtered Cu K<sub>α</sub> radiation ( $\lambda=1.5404 \text{ \AA}$ ) in the  $2\theta$  from 5° to 80° with high score plus software. Alternatively, data obtained from Fourier transform infrared spectroscopy (FTIR – Jasco 6100, Japan) of the developed HAp/G nanocomposite (pelletized in excess KBr) in the range of 4000–400 cm<sup>-1</sup> at room temperature assisted in understanding its active functionality. A Zeta potential (Zetasizer Nano S, Malvern Instruments, UK) measurement of HAp/G aqueous suspensions of different pH was helpful to monitor the electrochemical equilibrium at the interface and estimate the point of zero charge (PZC) of the HAp/G nanocomposite. Zeta potential was measured using a combination of Electrophoresis and Laser Doppler Velocimetry (sometimes called Laser Doppler Electrophoresis) techniques by applying an electrical field through gold-plated electrodes. Interestingly, these measurements succeeded to provide useful information regarding the adsorption of MB (a cationic pollutant) on the surface of the HAp/G nanocomposite in different media. Before measurements, HAp/G nanocomposite was dispersed in DI water (Milli-Q Millipore, Billerica, MA, USA) and the pH was adjusted using NaOH and HCl, to leave the suspension under ultrasonication (SB-120DTN, Taiwan) for 10 min.

## 2.2 Sorption study

### 2.2.1 Determination of the sorption capacity

The batch equilibrium technique was employed at room temperature. Different concentrations of MB solutions were prepared in DI water. Typically, a fixed amount of HAp/G nanocomposite was added to 100 mL of MB solution after a pH adjustment. The mixture was next shaken (Shaker, Heidolph, Unimax 1010, Germany) at 350 rpm for different durations. The (HAp/G) sorbent was then filtered by a 0.4  $\mu\text{m}$  syringe filter to pass the MB-containing filtrate for UV-Vis-NIR spectrophotometric (Cary 5000, Varian, England) analysis at an excitation wavelength of 633 nm. The equilibrium sorption capacity ( $q_e$ , mg g<sup>-1</sup>) of HAp/G, which is defined by the equilibrium amount (mg) of MB dye adsorbed per gram of sorbent was calculated using the general equation [38]:

$$q_e = \frac{(C_o - C_t)V}{M} \quad (1)$$

where  $C_o$  and  $C_t$  are the MB concentrations (mg L<sup>-1</sup>) in solution before and after adsorption,  $V$  is the solution volume (L) and  $M$  is the amount (g) of the sorbent employed in the adsorption experiment.

Also the removal efficiency,  $R$ , was calculated using the following equation:

$$R = \frac{(C_0 - C_t)}{C_0} \times 100 \% \quad (2)$$

### 2.2.2 Kinetics of adsorption

The kinetic progress of sorption processes was monitored by adding 0.05 g of HAp/G to 100 mL MB (200 mg L<sup>-1</sup>) solution and the mixture was shaken at room temperature for different durations (5–120 min). The same processing of separation and analysis was employed to estimate the sorption capacity ( $q_t$ , mg g<sup>-1</sup>) as a function of contact time ( $t$ , min) to represent the data according to pseudo-second-order reaction kinetics (Eq. 3) and evaluate  $q_e$  and the sorption rate constant ( $k$ , g mg<sup>-1</sup> min<sup>-1</sup>).

$$\frac{t}{q_t} = \frac{1}{kq_e^2} + \left(\frac{1}{q_e}\right)t \quad (3)$$

The sorption rate  $h$  (mg g<sup>-1</sup> min<sup>-1</sup>) was also calculated using the following equation [39]:

$$h = kq_e^2 \quad (4)$$

### 2.2.3 Effect of initial MB concentration

The influence of the initial MB concentration on the adsorption kinetics was also investigated where HAp/G (0.05 g) was added to aqueous MB containing solutions of various concentrations (25, 50, 100, 200, 300 and 500 mg L<sup>-1</sup>) commencing the same processing of separation and analysis. The Langmuir adsorption isotherm was then employed to understand the adsorption mechanism [40]. Langmuir isotherm proposes a monolayer adsorption of solutes on identical (same energy) active sites of heterogeneous surfaces according the following equation:

$$\frac{C_e}{q_e} = \frac{1}{bq_m} + \left(\frac{1}{q_m}\right) C_e \quad (5)$$

where  $q_m$  (mg g<sup>-1</sup>) is the maximum sorption capacity and  $b$  (L mg<sup>-1</sup>) is the Langmuir constant which correlates to the adsorption energy [40].

### 2.2.4 Effect of pH and sorbent dosage

The effect of pH (3–11) and the sorbent dosage (0.01 – 0.15 g) on the sorption capacity were evaluated to attain a convenient optimization for the sorption process.

## 2.3 Regeneration

The regeneration process of the HAp/G hybrid nanocomposite was sought by the end of the sorption experiment in order to dissolve MB dyes so that the composite may long-last executing the removal process. In this experiment, 0.1 g of HAp/G was added to 100 mL MB solution (200 mg L<sup>-1</sup>, pH = 5.5) under a continuous shaking for 90 min. The sorbent (HAp/G) residue was washed with deionized water and added to 200 mL Ca(NO<sub>3</sub>)<sub>2</sub>·4H<sub>2</sub>O solution (pH = 3.0) [41] and the mixture was

left for 2 h under magnetic stirring. After centrifugation, 0.08 g of this residue was dried and added to 80 mL 200 mg L<sup>-1</sup> MB solution (pH = 5.5) and the mixture was shaken for 90 min before measuring the MB's equilibrium concentration.

### 3. RESULTS AND DISCUSSION

#### 3.1 Materials characterization

Typical TEM images of GO and HAp/G crystals are shown in Fig. 1A and B. The as-synthesized GO appeared in large two-dimensional nanosheets. In agreement with previous investigations, the GO nanosheets (Fig. 1A) were not perfectly flat but exhibited intrinsic roughening and out-of-plane deformations (wrinkles) with one or few layer sheet structure [42, 43]. The multilayered structure in GO may represent the parts that either have not been fully exfoliated or have restacked together due to capillary, electrostatic interaction and the Van der Waals forces during the dispersion process [42, 43]. Figure 1B, on the other hand, evokes a perfect distribution of hydroxyapatite mostly in nanorods (ca. 5 nm in diameter and 20-50 nm in length) on graphene nanosheets; allowing the formation of a stable HAp/G hybrid nanocomposite (of a large surface area) compiling, hopefully, the unique physical, chemical and mechanical properties of graphene and featuring the high adsorption capacity of HAp. Figure 1C represents the selected area electron diffraction (SAED) pattern from the monolayer region of the GO film (Fig. 1A). Strikingly, clear diffraction spots were observed; recommending a highly crystalline 6-fold pattern consistent with a hexagonal lattice (spots could be labeled according to the Miller-Bravais *hkil* notation) [44]. Alternatively, the SAED pattern of HAp/G composite (Fig. 1D) exhibited polycrystalline diffraction rings where spots identifying the (002), (121), (030), (112) planes of HAp crystals could only be observed. The high resolution TEM image for HAp in the HAp/G composite (Fig. 1E) appeared highly crystalline with d-spacing (between the columns of atoms) of 2.81, 3.08 and 3.42 °Å. This agreed well with the XRD results (JCPDS no.00-064- 0738) of highly crystalline HAp. The EDX analyses in Fig. 1F estimated the relative elemental composition of the bulk materials of GO and HAp/G. In case of GO, only the carbon and oxygen peaks appeared. However, for HAp/G, the carbon, oxygen, calcium and phosphorus peaks appeared with a stoichiometric ratio of Ca/P equal to 1.67; exactly in the same starting preparation ratio to infer a successful optimized HAp's preparation. Comparing the EDX analyses also highlighted the enrichment of HAp/G composite with oxygen from the hydroxide and phosphate groups of HAp. This can definitely influence the hydrophilic nature and surface charging of the composite in different electrolytes.

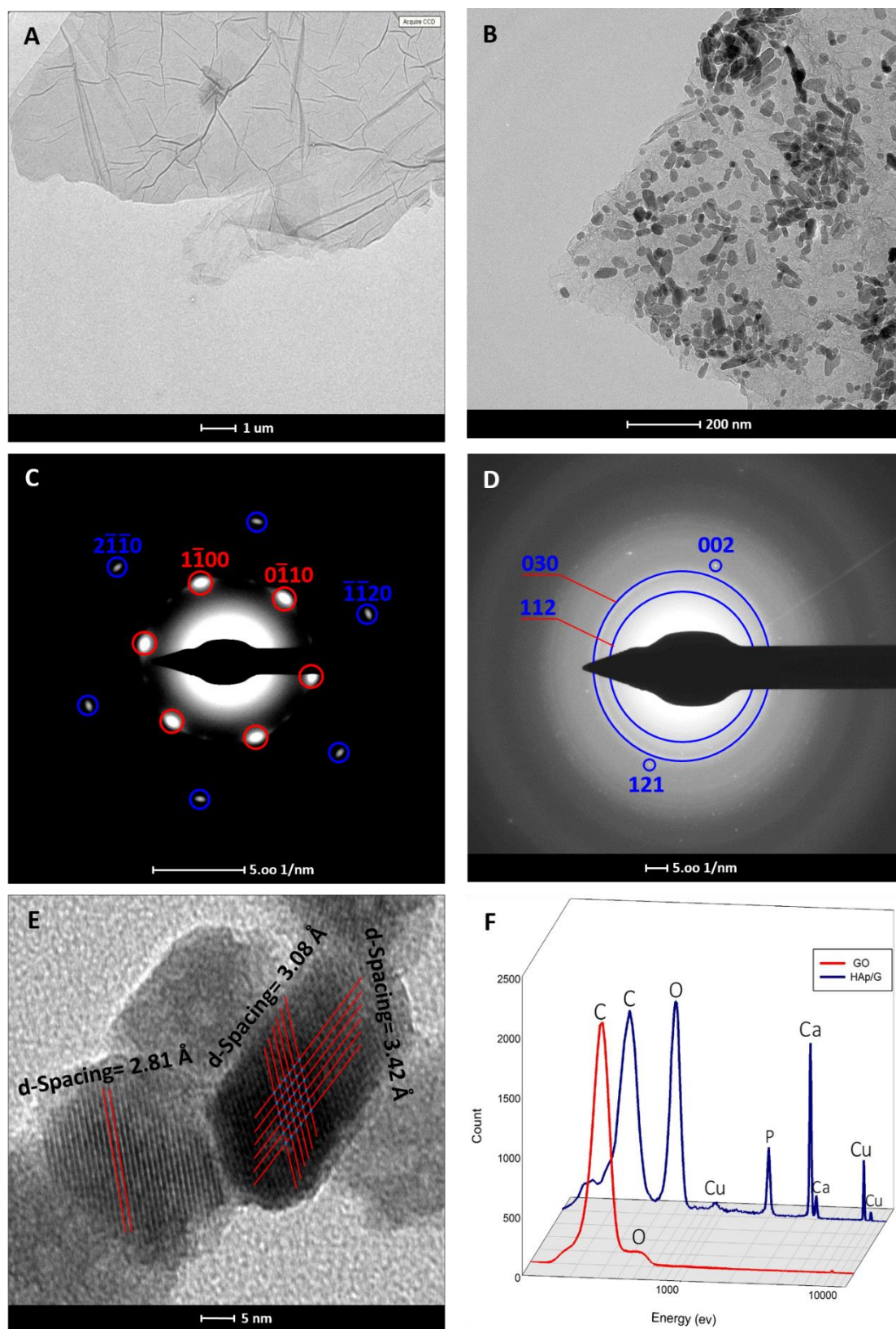


**Figure 1.** TEM images of GO (A) and HAp/G (B), Selected area electron diffraction patterns for GO (C) and HAp/G (D), HR-TEM image of HAp on HAp/G composite (E) and comparative EDX analyses of GO and HAp/G (F).

The as-prepared GO and HAp/G nanocomposite were subjected to XRD analysis in order to inspect their crystallography. The XRD pattern of GO in Fig. 2 indicates, interestingly, a single diffraction peak at  $2\theta$  of  $11.05^\circ$ , which was assigned to the (0 0 1) plane of GO with interlayer spacing  $d_{(001)} = 0.817$  nm [45]. On the other hand, the diffraction pattern of HAp/G composite exhibited several diffraction peaks at  $2\theta$  of  $25.95^\circ$ ,  $31.76^\circ$ ,  $32.20^\circ$ ,  $32.96^\circ$ ,  $46.72^\circ$  and  $49.53^\circ$ , corresponding, respectively, to the (0 0 2), (1 2 1), (1 1 2), (0 3 0), (2 2 2) and (1 2 3) crystal planes of HAp (JCPDS card No.00-064- 0738). This suggested precisely the high crystallinity of HAp in the HAp/G composite. Surprisingly, the diffraction peak of graphene which typically appears at  $2\theta$  of  $25.3^\circ$  was missing perhaps due to the amorphous nature of graphene that imparted a weakness and broadness for this peak; hiding it within the perfectly crystalline diffraction pattern of HAp [46]. Hence, if one compared the diffraction patterns of HAp/G and pure HAp [19, 20], they would look similar. The superior scattering strength of HAp compared to graphene may also account for missing the diffraction pattern of graphene in the HAp/G composite [47].

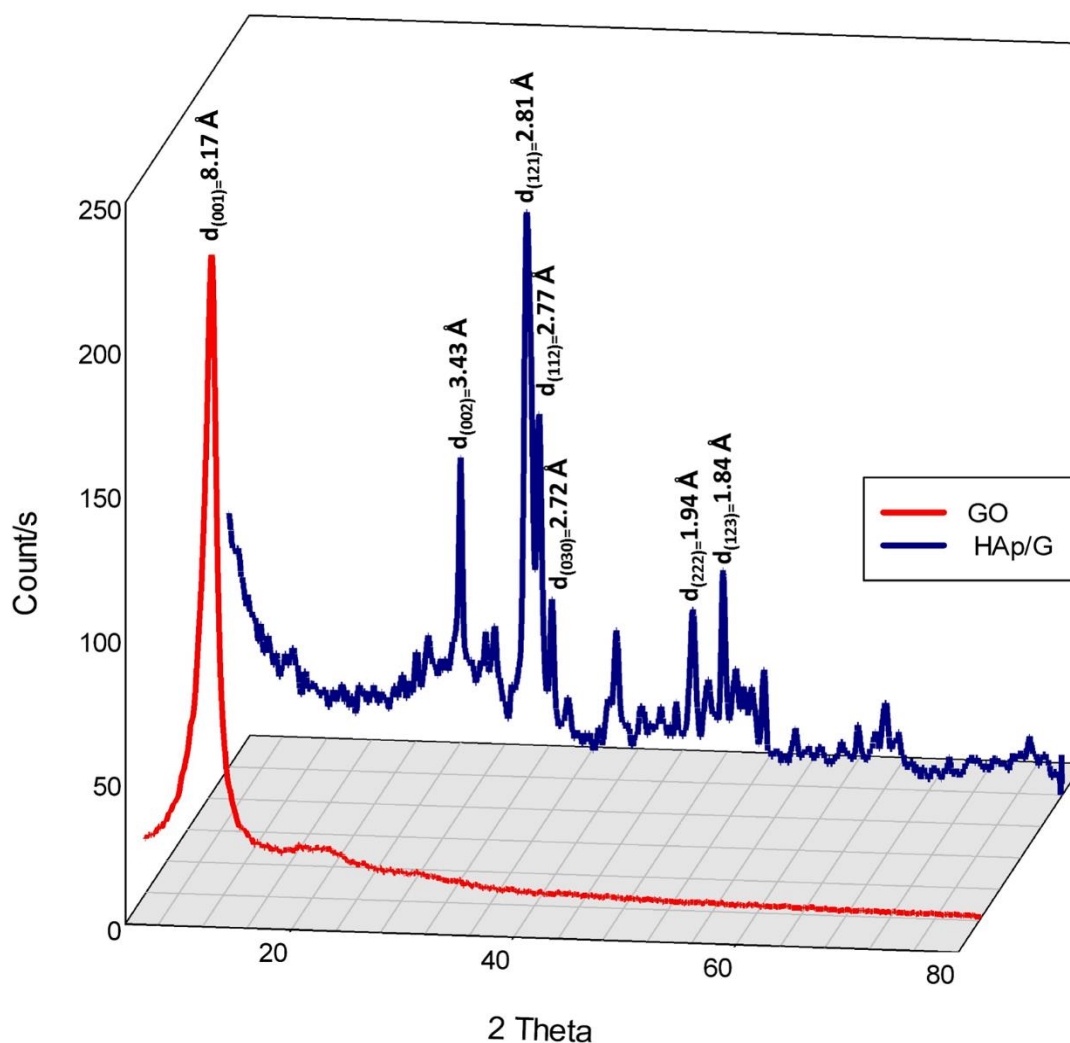


**Figure 2.** XRD diffraction patterns of GO and HAp/G. Samples were prepared as described in the experimental section.

The FTIR spectroscopy was further employed to interpret the functionality of the as-prepared nanocomposite. For referencing, the FTIR spectrum of GO in Fig. 3 indicated the presence of a major peak at ca.  $3400\text{ cm}^{-1}$  corresponding to the symmetric stretching vibration of absorbed water molecules and surface  $\text{-OH}$  vibration of surface carbocyclic rings [48]. It also depicts the existence of different oxygenated bondings in relevance to the absorptions retained at  $1729$ ,  $1220$  and  $1053\text{ cm}^{-1}$  which could likely be assigned to the  $\text{C=O}$ ,  $\text{C-O}$  (epoxy) and  $\text{C-O}$  (alkoxy) stretching vibrations, respectively [49]. In addition, the strong peak at  $1625\text{ cm}^{-1}$  corresponded to the  $\text{sp}^2$  hybridized  $\text{C=C}$  stretching vibration of the unoxidized graphitic domains or the bending vibration of the absorbed water molecules [50]. All these vibrations have proven the abundance of carboxyl, hydrophilic hydroxyl and epoxide groups in GO [51]. On the other hand, the FTIR spectrum of HAp/G composite displayed a noticeable decrease in the intensity of oxygenated bands which concurred with the reduction of GO. The disappearance of the  $\text{C=O}$  peak at  $1729\text{ cm}^{-1}$  of GO in the HAp/G composite reinforced this assumption. The intense peaks at  $566$  and  $601\text{ cm}^{-1}$  in the HAp/G composite corresponded to the bending vibration of the  $\text{O-P-O}$  in the  $\text{PO}_4^{3-}$  groups [52]. The featured band at  $1623\text{ cm}^{-1}$  arising from the  $\text{C=C}$  stretching vibration of the graphene layer backbone [53]. The asymmetric stretching vibrations of  $\text{P-O}$  bonding in the  $\text{PO}_4^{3-}$  groups at  $1092$  and  $1035\text{ cm}^{-1}$  confirmed the successful formation of HAp [54]. The appearance of most characteristic absorption peaks of HAp and graphene in the absorption spectrum of HAp/G suggested the successful formation of the HAp/G hybrid composite.

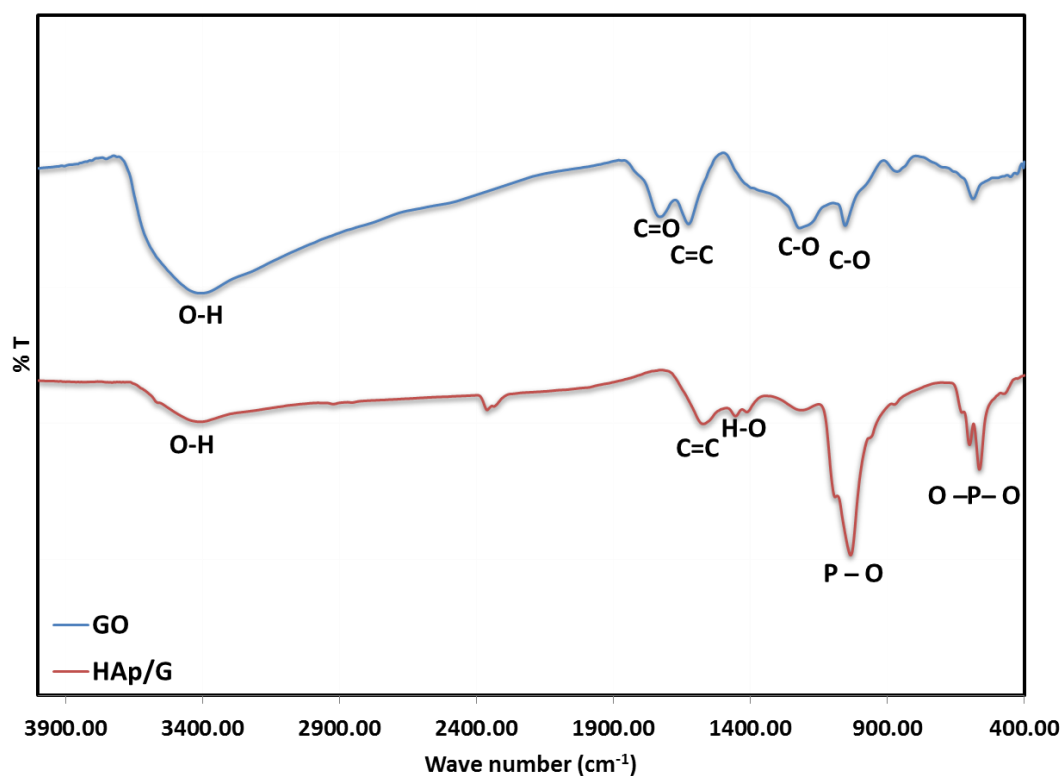


**Figure 3.** FTIR spectra of GO and HAp/G. Samples were prepared as described in the experimental section.

The materials characterization continued to evaluate the PZC of the HAp/G nanocomposite in aqueous solutions which denotes the pH at which the nanocomposite exhibited zero net electrical charge at the surface. With Zeta-potential (electrokinetic potential) measurements (Fig. 4), the PZC of the HAp/G nanocomposite in aqueous solutions was 2.3. Now, at pH lower than 2.3, the HAp/G composite is expected to carry a positive charge, and the opposite (carrying a negative charge) is true at pH higher than 2.3. Understanding the nature of binding MB to HAp/G will definitely consider these charging domains, and the adsorption capacity is expected to vary accordingly. Recalling the classification of MB as a cationic dye predicts a removal superiority at the HAp/G composite at high pH values (where the composite's surface is negatively charged) which is driven electrostatically [55]. On the other hand, below pH of 2.3 (the adsorbent is positively charged), the MB's removal may proceed according to a cation exchange mechanism.

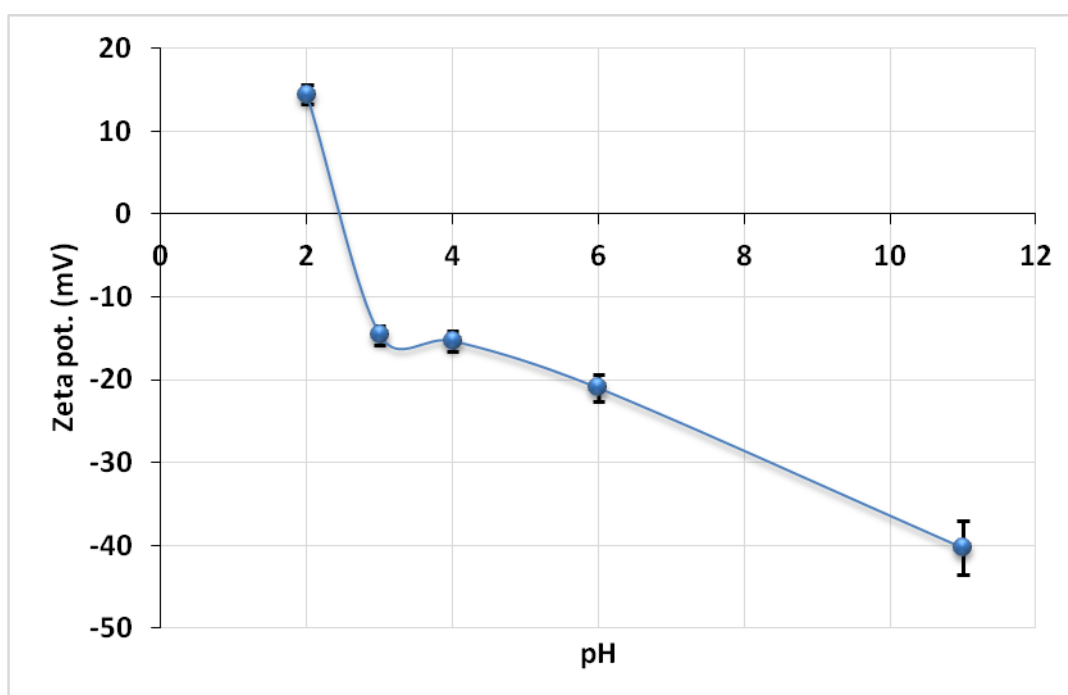


**Figure 4.** Zeta-potential measurements for (0.1 w/v %) HAp/G suspension in water at different pH and 25°C.

### 3.2 Sorption study

#### 3.2.1 Effect of contact time

The adsorption isotherm of MB on HAp/G nanocomposite is displayed in Fig. 5A in a batch experiment using 0.05 g HAp/G and an initial MB concentration of 200 mg L<sup>-1</sup> at pH of 5.5 and room temperature. It indicates a fast early (within ~ 20 min) removal of MB followed by a much slower step before reaching equilibrium. A contact time of 3 h was enough to saturate the HAp/G's surface with MB. The rate of MB sorption on the HAp/G's surface was estimated using the linear form of a pseudo-second-order kinetic model (Fig. 5B). With this treatment, the pseudo-second-order constants ( $k$ ,  $q_e$ ,

and  $h$ ) of HAp/G could be estimated using equations 3 and 4 (see Table 1). Interestingly, the pseudo-second-order kinetic model was ideal for the adsorption of MB on HAp/G nanocomposite with a regression coefficient approaching almost one [56]. This may infer that the overall removal process of MB at the HAp/G composite was mainly controlled by the adsorption step.

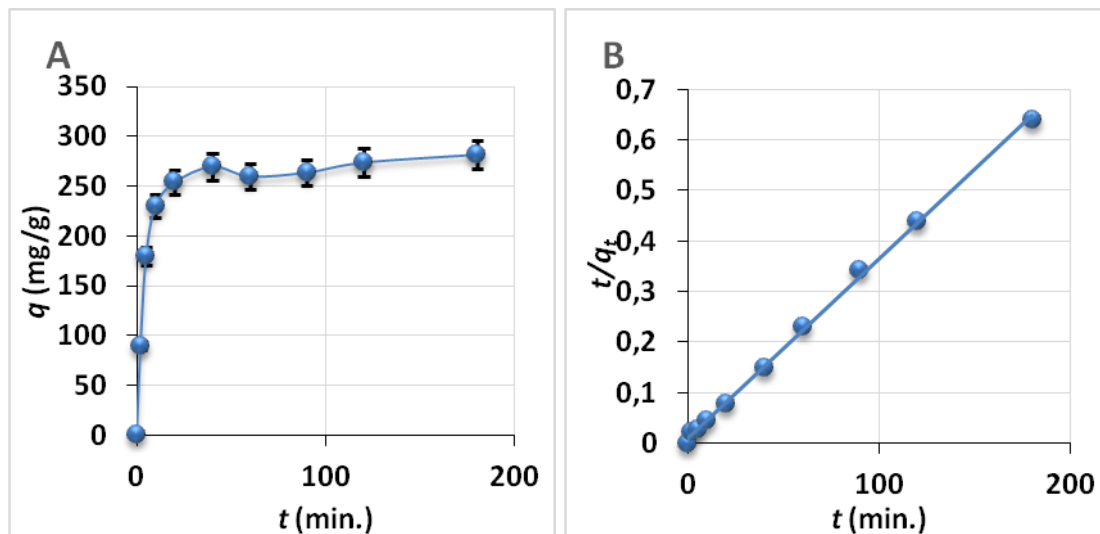


**Figure 5.** Kinetics of MB (200 mg/L) adsorption on 0.05 g HAp/G composite (A) and a linear fitting of experimental data using pseudo-second-order kinetic model (B).

**Table 1.** Pseudo-second-order kinetic data of methylene blue sorption on HAp/G nanocomposite.

Sorbents	$k(g/mg.min)$	$q_e(mg/g)$	$h(mg/g.min)$	$R^2$
HAp/G	0.340	285.714	98.039	0.999

### 3.2.2 Effect of initial MB concentration

The investigation is steered next to investigate the impact of the MB’s initial concentration on the sorption kinetics. Several solutions containing different concentrations of MB were involved in the sorption experiment with 0.05 g HAp/G and the regular procedure to estimate  $q_e$  was followed. Figure 6 indicates a significant increase in  $q_e$  of MB at the HAp/G composite with the initial MB concentration. Interestingly,  $q_e$  jumped from 49.9 to 332.0 mg/g with increasing the initial MB concentration from 25 to 500 mg L<sup>-1</sup>. Typical adsorption isotherms usually correlate a dependence of the equilibrium concentration of adsorbate (as MB) at the surface of adsorbent (HAp/G) with its equilibrium concentration in the bulk solution. That may explain the observed increase in  $q_e$  with the initial concentration of MB. High concentrations of MB may support a favorable mass diffusion of MB to active adsorption sites of HAp/G composites to ultimately increase  $q_e$ . However, surprisingly, the removal efficiency of MB at the HAp/G composite did not follow the same pattern. Superb removal efficiency (almost 100 %) was achieved for solutions containing MB’s initial concentrations less than 50 mg L<sup>-1</sup>. The efficiency decreased with the MB’s initial concentration to reach 33 % in solutions

containing 500 mg L<sup>-1</sup> MB. Actually, Eq. 2 is able to predict this contradiction where the removal efficiency depended inversely on the initial concentration as it depended directly on  $q_e$ . However, it seems the increase in  $q_e$  accompanying the increase in the MB's initial concentration could not surpass its associated influence to decrease the removal efficiency. This rationalization assumes the availability of abundant active sites at the HAp/G composite for adsorbing MB. However, if this was not valid and the active sites were deficient (particularly if a small amount of HAp/G composite was employed), a quick saturation of HAp/G composite with MB would happen. That would pertain a superior removal efficiency (approaching 100 %) at low MB's initial concentrations which would decrease accordingly by increasing the MB's initial concentration for lacking sufficient active sites for adsorption [57]. Being the sorption process of MB on HAp/G reversible will add more complications for addressing the role of the initial concentration of MB on the removal efficiency.

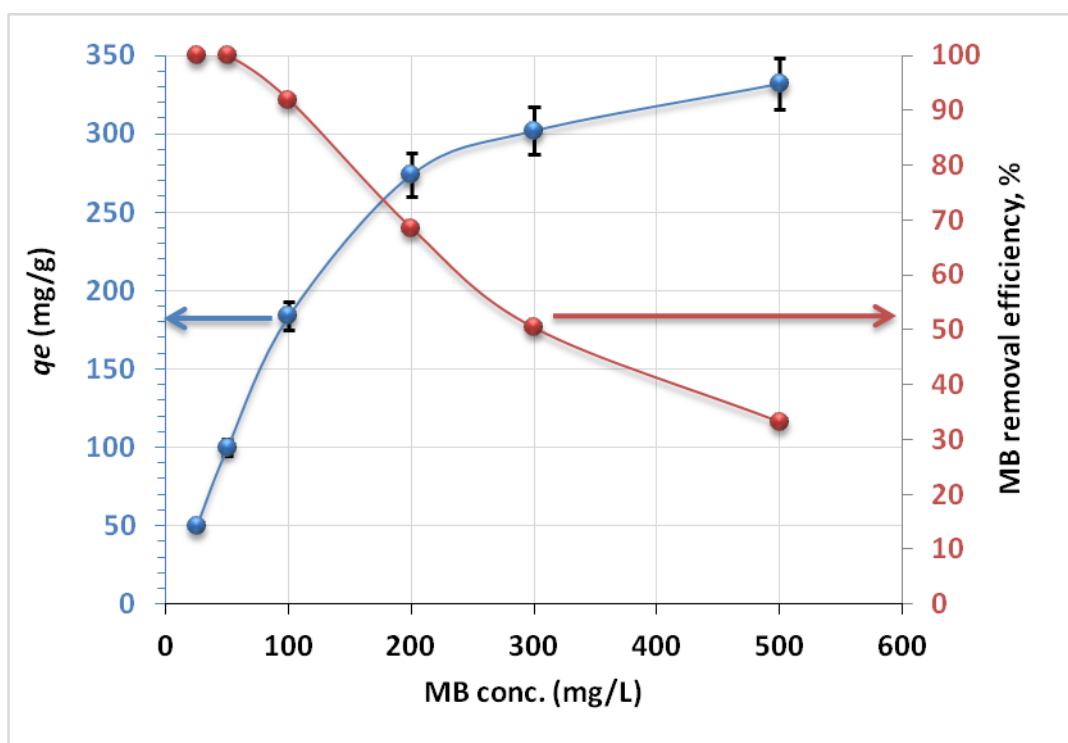


**Figure 6.** Effect of the MB's initial concentration on the equilibrium sorption capacity and removal efficiency of MB by the HAp/G composite (pH=5.5, adsorbent dosage=0.05 g).

Kinetically, the sorption process was modeled with Langmuir isotherm (Eq. 5) [58]. Langmuir's arguments was completely fitted with our experimental results ( $R^2=0.99$ ); considering a monolayer adsorption process in heterogeneous systems and assuming the participation of definite active sites in the sorption process with 1:1 ratio. It also ignores interactions between neighboring adsorbates regardless of their overall surface coverage. Figure 7 shows the relation of  $C_e/q_e$  as a function of  $C_e$  according to Langmuir isotherm from which  $q_m$  was calculated to be 333.3 mg/g, while Langmuir constant (b) was 0.11 L/ mg. The maximum sorption capacity ( $q_m$ ), represented the monolayer coverage of HAp/G with MB [59]. Table 2 providing a simple comparison of  $q_m$  of MB at HAp/G and

at other sorbent materials indicates a comparative superiority of HAp/G toward MB removal [60-69].

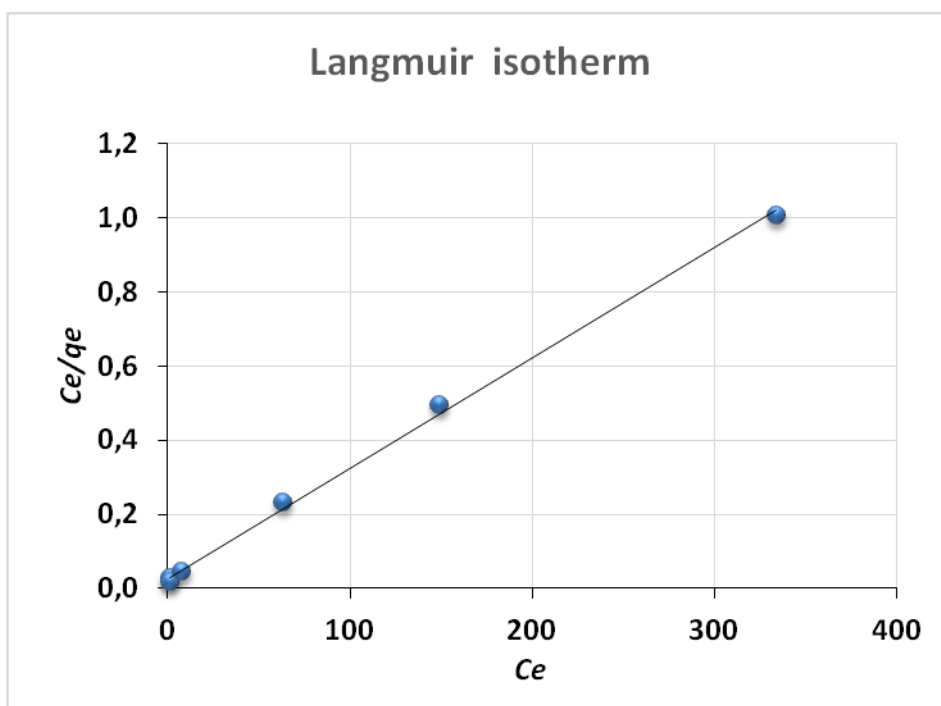


**Figure 7.** Langmuir sorption isotherm for the adsorption of MB onto HAp/G (pH=5.5, adsorbent dosage=0.05 g).

**Table 2.** Comparison of sorption capacities for MB with various sorbents.

Sorbents	Adsorption capacity, $q_m$ (mg/g)	Reference
Graphene-carbon nanotube	65.79	[54]
Chitosan-clay composite	259.80	[55]
NaOH treated diatomite	27.86	[56]
Graphene oxide/calcium alginate composites	181.81	[57]
Jiangsu palygorskite (JSHS)	158.03	[58]
Defatted algal biomass (DAB)	7.73	[59]
Keratin nanofibrous membranes	170.00	[60]
Montmorillonite clay modified with iron oxide (MtMIO)	71.12	[61]
Vegetal fiber activated carbons	33.70	[62]
Date Palm Leaves Powder (DPLP)	58.14	[63]
Hydroxyapatite/graphene nanocomposite	333.30	Present work

### 3.2.3 Effect of pH

The influence of pH on the sorption process of MB on HAp/G was studied as a function of pH (3–11) (see Fig. 8). As we mentioned early, changing the pH is expected to influence the bonding mechanism and the sorption capacity of MB on HAp/G nanocomposite by changing the electrical

surface charge of HAp/G composite. It might also affect the number of active sites available for this adsorption process [70]. In this investigation, the MB uptake increased much with pH. This can likely be described in view of a mutual competition between protons ( $H^+$ ) and the cationic functional groups of MB for the participation on the sorption process on HAp/G. At low pH, protons are plenty and they could occupy a large number of active adsorption sites of HAp/G to leave few sites available for MB's removal. The accommodation of protons at the HAp/G composite impart a cumulative positive charge at the surface which induces an electrostatic repulsion with cationic groups of MB; reducing the sorption capacity [71, 72]. On the other hand, at high pH, the proton competition disappears and the HAp/G acquires a negative electrical charge that drives electrostatically the attraction with positively charged groups of MB to increase the MB's removal efficiency [73]. This was very much consistent with the zeta potential measurements that recommended a pH of 2.3 as the PZC. Below this pH, the HAp/G's surface will be positively charged, which encounters the sorption process of cationic dyes as MB. Above pH of 2.3, the opposite occurs and the sorption of MB will be enhanced at the HAp/G nanocomposite.

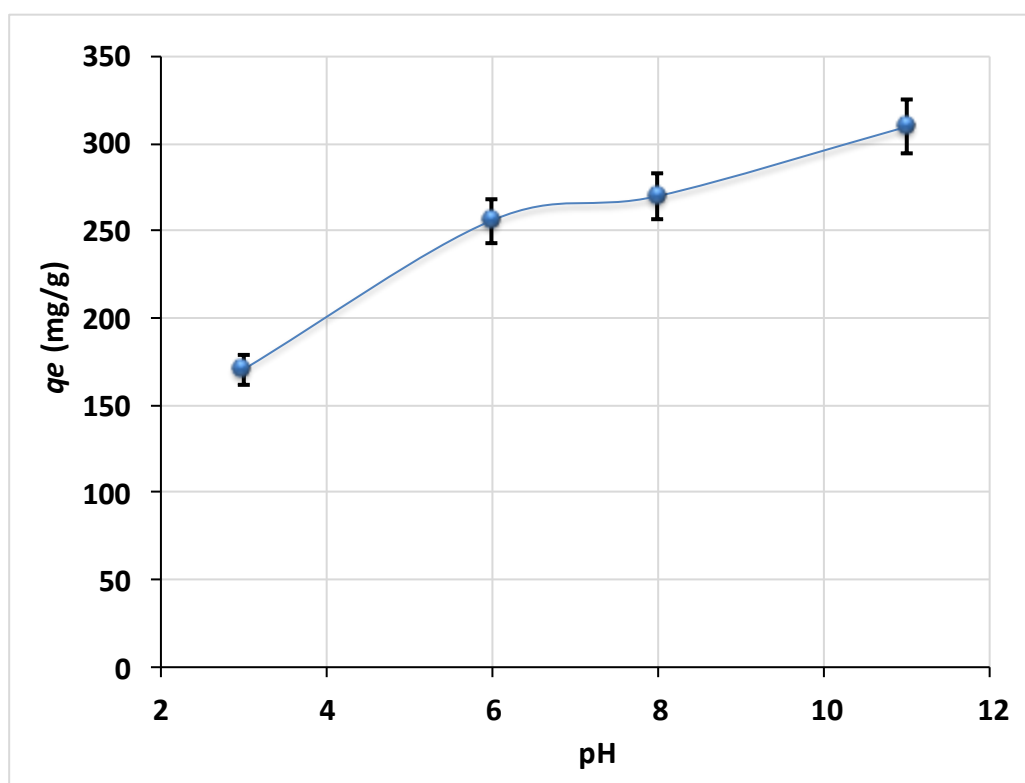


**Figure 8.** Effect of pH on the sorption capacity of MB by HAp/G composite (initial concentration 200 mg/L, adsorbent dosage 0.05 g).

### 3.2.4 Adsorbent dosage

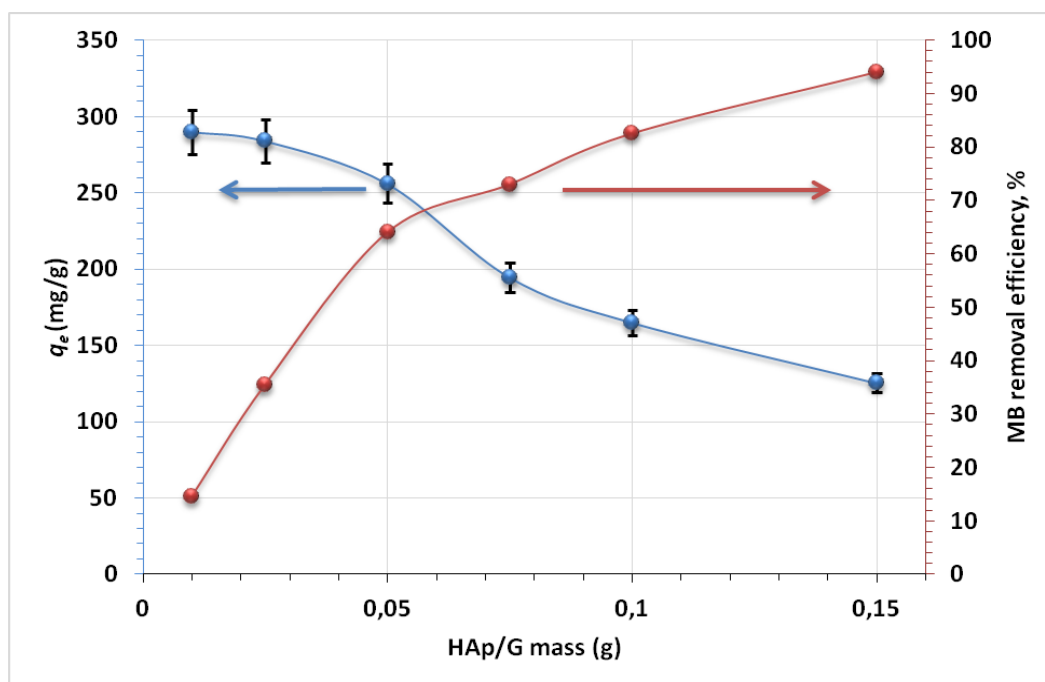


**Figure 9.** Effect of adsorbent dosage of HAp/G on the MB's uptake and removal efficiency (initial MB's concentration was 200 mg/L, pH=5.5).

Optimizing the HAp/G dosage involved in the sorption process is also important to minimize the chemicals added in wastewater treatment. Figure 9 aims at elucidating the impact of the HAp/G dosage on the adsorption uptake. As anticipated, the MB sorption increased rapidly with the HAp/G dosage perhaps due to the corresponding increase of the active sites available for the MB removal. Interestingly, 0.15 g of HAp/G could impart an MB's removal efficiency of 92%. Although the MB removal efficiency increased with the HAp/G dosage, the sorption capacity, which normalizes the MB uptake to the HAp/G dosage, decreased [40]. Therefore, one should customize the process to obtain the highest possible removal efficiency for MB with the least amount of the HAp/G dosage.

### 3.3 HAp/G's regeneration

Of the important features of proper sorbents is its ability to be regenerated easily. The regeneration of HAp/G after adsorbing MB was sought in  $\text{Ca}^{2+}$  containing acidic solutions (pH=3) principally to get rid the adsorbed MB and to compensate dissolved calcium ions which ultimately reactivated the HAp/G composite for further processing. Promising results with a recovery approaching 69% was obtained. Research is still running to improve this efficiency. We believe the varying the composition and temperature of the regeneration solution together with allowing the regeneration to last longer will definitely improve the regeneration efficiency.

#### 4. CONCLUSION

This investigation highlights the effectiveness of hydroxyapatite/graphene (HAp/G) hybrid nanocomposite in the adsorptive removal of methylene blue (MB) dye from aqueous solutions in wastewater treatments. The adsorption process was investigated as a function of the contact time, initial MB's concentration, pH and sorbent dosage. The kinetics of the sorption process could be fitted to a pseudo-second-order reaction model where the sorption capacity of MB by HAp/G nanocomposite increased with the initial MB's concentration. Langmuir adsorption isotherm has been employed to evaluate the adsorption behavior, where a maximum adsorption capacity for HAp/G of 333.3 mg/g was obtained. Interestingly, the MB sorption by HAp/G increased with pH and HAp/G dosage while the sorption capacity decreased with the HAp/G dosage. Fortunately, a regeneration efficiency of 69% could be achieved for the HAp/G after the adsorption process by treating it in  $\text{Ca}^{2+}$  containing aqueous slightly acidic solutions.

#### References

1. IFAD. *Water: A precious resource under stress*. Available from: <https://www.ifad.org/web/guest/water>
2. M. Bilal, M. Asgher, M. Iqbal, H. Hu and X. Zhang, *Int. J. Biol. Macromol.* 89 (2016) 181.
3. Y. Li, W. Nie, P. Chen and Y. Zhou. *Colloids Surf. A* 499 (2016) 46.
4. H. Karaer and İ. Kaya. *Microporous Mesoporous Mater.* 232 (2016) 26.
5. Z. Wu and D. Zhao. *Chem. Commun.* 47 (2011) 3332.
6. M. A. Mohammed, A. Shitu and A. Ibrahim. *Res. J. Chem. Sci.* 4 (2014) 91.
7. J.-L. Gong, Y.-L. Zhang, Y. Jiang, G.-M. Zeng, Z.-H. Cui, K. Liu, C.-H. Deng, Q.-Y. Niu, J.-H. Deng and S.-Y. Huan. *Appl. Surf. Sci.* 330 (2015) 148.
8. G. Crini. *Bioresour. Technol.* 97 (2006) 1061.
9. B. Shi, G. Li, D. Wang, C. Feng and H. Tang. *J. Hazard. Mater.* 143 (2007) 567.
10. M. Rafatullah, O. Sulaiman, R. Hashim and A. Ahmad. *J. Hazard. Mater.* 177 (2010) 70.
11. T. Robinson, G. McMullan, R. Marchant and P. Nigam. *Bioresour. Technol.* 77 (2001) 247.
12. M. J. Ahmed. *J. Environ. Chem. Eng.* 4 (2016) 89.
13. E. I. El-Shafey, S. N. F. Ali, S. Al-Busafi and H. A. J. Al-Lawati. *J. Environ. Chem. Eng.* 4 (2016) 2713.
14. Z. Zou, K. Lin, L. Chen and J. Chang. *Ultrason. Sonochem.* 19 (2012) 1174.
15. S. Saber-Samandari, S. Saber-Samandari and M. Gazi. *React. Funct. Polym.* 73 (2013) 1523.
16. D. C. Manatunga, R. M. de Silva, K. M. Nalin de Silva, N. de Silva and E. V. A. Premalal. *R. Soc. Open Sci.* 5 (2018)
17. U. Vijayalakshmi, K. Prabakaran and S. Rajeswari. *J. Biomed. Mater. Res., Part A* 87 (2008) 739.
18. N. N. C. Isa, Y. Mohd and N. Yury. *APCBEE Proc.* 3 (2012) 46.
19. T. A. Salah, A. M. Mohammad, M. A. Hassan and B. E. El-Anadouli. *J. Taiwan Inst. Chem. Eng.*, 45 (2014) 1571.
20. A. M. Mohammad, T. A. Salah Eldin, M. A. Hassan and B. E. El-Anadouli. *Arab. J. Chem.*, 10 (2017) 683.
21. M. S. El-Deab, G. A. El-Nagar, A. M. Mohammad and B. E. El-Anadouli. *J Power Sources*, 286 (2015) 504.
22. G. A. El-Nagar, A. M. Mohammad, M. S. El-Deab, T. Ohsaka and B. E. El-Anadouli. *J Power Sources*, 265 (2014) 57.

23. M. S. El-Deab, A. M. Mohammad, G. A. El-Nagar and B. E. El-Anadouli. *J. Phys. Chem. C*, 118 (2014) 22457.
24. A. M. Mohammad, A. I. Abdelrahman, M. S. El-Deab, T. Okajima and T. Ohsaka. *Colloids Surf. A Physicochem. Eng. Asp.*, 318 (2008) 78.
25. H. Chang and H. Wu. *Energy Environ. Sci.* 6 (2013) 3483.
26. S. C. Ray, in *Application and Uses of Graphene, in Applications of Graphene and Graphene-Oxide Based Nanomaterials*, p. 1-38, William Andrew Publishing: Oxford. (2015).
27. Y. Zhu, S. Murali, W. Cai, X. Li, J. W. Suk, J. R. Potts and R. S. Ruoff. *Adv. Mater.* 22 (2010) 3906.
28. X. Du, I. Skachko, A. Barker and E. Y. Andrei. *Nat. Nanotechnol.* 3 (2008) 491.
29. X. Huang, Z. Yin, S. Wu, X. Qi, Q. He, Q. Zhang, Q. Yan, F. Boey and H. Zhang. *Small.* 7 (2011) 1876.
30. C. Lee, X. Wei, J. W. Kysar and J. Hone. *Sci.* 321 (2008) 385.
31. A. A. Balandin, S. Ghosh, W. Bao, I. Calizo, D. Teweldebrhan, F. Miao and C. N. Lau. *Nano Lett.* 8 (2008) 902.
32. V. Chandra, J. Park, Y. Chun, J. W. Lee, I.-C. Hwang and K. S. Kim. *ACS Nano.* 4 (2010) 3979.
33. L. Fan, C. Luo, M. Sun and H. Qiu. *J. Mater. Chem.* 22 (2012) 24577.
34. Z. Sui, Q. Meng, X. Zhang, R. Ma and B. Cao. *J. Mater. Chem.* 22 (2012) 8767.
35. W. S. Hummers and R. E. Offeman. *J. Am. Chem. Soc.* 80 (1958) 1339.
36. M. A. Farghali, T. A. Salah El-Din, A. M. Al-Enizi and R. M. El Bahnasawy. *Int. J. Electrochem. Sci.* 10 (2015) 529.
37. G. Bharath, R. Madhu, S.-m. Chen, V. Veeramani, A. Balamurugan, D. Mangalaraj, C. Viswanathan and N. Ponpandian. *J. Mater. Chem. B.* 3 (2015) 1360.
38. W. Zheng, X.-m. Li, Q. Yang, G.-m. Zeng, X.-x. Shen, Y. Zhang and J.-j. Liu. *J. Hazard. Mater.* 147 (2007) 534.
39. Y. S. Ho and G. McKay. *Process Biochem.* 34 (1999) 451.
40. K. G. Bhattacharyya and S. S. Gupta. *J. Colloid Interface Sci.* 310 (2007) 411.
41. S. Sugiyama, K. Fukuta and K.-I. Sotowa. *J. Colloid Interface Sci.* 299 (2006) 270.
42. D. Chen, R. Yi, S. Chen, T. Xu, M. L. Gordin, D. Lv and D. Wang. *Mater. Sci. Eng., B.* 185 (2014) 7.
43. D. Wang, D. Choi, J. Li, Z. Yang, Z. Nie, R. Kou, D. Hu, C. Wang, L. V. Saraf, J. Zhang, I. A. Aksay and J. Liu. *ACS Nano.* 3 (2009) 907.
44. N. R. Wilson, P. A. Pandey, R. Beanland, R. J. Young, I. A. Kinloch, L. Gong, Z. Liu, K. Suenaga, J. P. Rourke, S. J. York and J. Sloan. *ACS Nano.* 3 (2009) 2547.
45. J. Lavanya, N. Gomathi and S. Neogi. *Mater. Res. Express.* 1 (2014) 025604.
46. J. H. Lee, Y. C. Shin, S.-M. Lee, O. S. Jin, S. H. Kang, S. W. Hong, C.-M. Jeong, J. B. Huh and D.-W. Han. *Sci. Rep.* 5 (2015) 18833.
47. A. Rajesh, G. Mangamma, T. N. Sairam, S. Subramanian, S. Kalavathi, M. Kamruddin and S. Dash. *Mater. Sci. Eng.* 76 (2017) 203.
48. Y. Qi, N. Du, H. Zhang, P. Wu and D. Yang. *J. Power Sources.* 196 (2011) 10234.
49. X. Sun and Y. Li. *Angew. Chem., Int. Ed.* 43 (2004) 597.
50. C. Chen, Q. Ru, S. Hu, B. An, X. Song and X. Hou. *Electrochim. Acta.* 151 (2015) 203.
51. Y. Xu, H. Bai, G. Lu, C. Li and G. Shi. *J. Am. Chem. Soc.* 130 (2008) 5856.
52. F. Ren, Y. Leng, R. Xin and X. Ge. *Acta Biomater.* 6 (2010) 2787.
53. F. Gao, Q. Wang, N. Gao, Y. Yang, F. Cai, M. Yamane, F. Gao and H. Tanaka. *Biosens. Bioelectron.* 97 (2017) 238.
54. X. Yang, Y. Wang, X. Huang, Y. Ma, Y. Huang, R. Yang, H. Duan and Y. Chen. *J. Mater. Chem.* 21 (2011) 3448.
55. S. Foorginezhad and M. M. Zerafat. *Ceram. Int.* 43 (2017) 15146.
56. Y. Wang, L. Hu, G. Zhang, T. Yan, L. Yan, Q. Wei and B. Du. *J. Colloid Interface Sci.* 494

- (2017) 380.
57. Z. Aksu and S. Tezer. *Process Biochem.* 40 (2005) 1347.
  58. K. Lin, J. Pan, Y. Chen, R. Cheng and X. Xu. *J. Hazard. Mater.* 161 (2009) 231.
  59. T. Suzuki, T. Hatsushika and M. Miyake. *J. Chem. Soc., Faraday Trans. 1.* 78 (1982) 3605.
  60. P. Wang, M. Cao, C. Wang, Y. Ao, J. Hou and J. Qian. *Appl. Surf. Sci.* 290 (2014) 116.
  61. M. Auta and B. H. Hameed. *Chem. Eng. J.* 237 (2014) 352.
  62. J. Zhang, Q. Ping, M. Niu, H. Shi and N. Li. *Appl. Clay Sci.* 83–84 (2013) 12.
  63. Y. Li, Q. Du, T. Liu, J. Sun, Y. Wang, S. Wu, Z. Wang, Y. Xia and L. Xia. *Carbohydr. Polym.* 95 (2013) 501.
  64. Y. Zhang, W. Wang, J. Zhang, P. Liu and A. Wang. *Chem. Eng. J.* 262 (2015) 390.
  65. T. Sarat Chandra, S. N. Mudliar, S. Vidyashankar, S. Mukherji, R. Sarada, K. Krishnamurthi and V. S. Chauhan. *Bioresour. Technol.* 184 (2015) 395.
  66. A. Aluigi, F. Rombaldoni, C. Tonetti and L. Jannoke. *J. Hazard. Mater.* 268 (2014) 156.
  67. L. Cottet, C. A. P. Almeida, N. Naidek, M. F. Viante, M. C. Lopes and N. A. Debacher. *Appl. Clay Sci.* 95 (2014) 25.
  68. H. Cherifi, B. Fatiha and H. Salah. *Appl. Surf. Sci.* 282 (2013) 52.
  69. M. Gouamid, M. R. Ouahrani and M. B. Bensaci. *Energy Procedia* 36 (2013) 898.
  70. O. Krivosheeva, A. Dédinaité and P. M. Claesson. *J. Colloid Interface Sci.* 379 (2012) 107.
  71. C. Namasivayam and K. Ranganathan. *Environ. Technol.* 16 (1995) 851.
  72. S. Doyurum and A. Çelik. *J. Hazard. Mater.* 138 (2006) 22.
  73. W. G. Breck. *J. Chem. Educ.* 58 (1981) A382.